Micromechanical Modelling of Elastic Wave Velocity Variations toward the failure of Brittle Rocks

A. Guggisberg[1], F. Paglialunga[1], A. Nicolas[2], M. Violay [1], F. X. Passelègue[1,3]

[1]Laboratory of Experimental Rock Mechanics (LEMR), École polytechnique fédérale de Lausanne (EPFL) Station 18, CH-1015 Lausanne, Switzerland
[2]Bureau Veritas Marine & Offshore, Paris La Défense, France
[3]Experimental SEIsmology LAboratory (ESEILA), Université de Côte d'Azur, UMR7329, Nice, France

Key Points:

- We studied the influence of confining pressure on stress induced anisotropy in crustal rocks.
- We developed a micromechanical model allowing to predict the evolution of elastic velocities toward the failure of brittle rocks.
- The off-fault dissipated energy is consistent with the evolution of the stiffness tensor due to micro-cracks propagation.

Corresponding author: Antoine Guggisberg, `antoine.guggisberg@epfl.ch`

Abstract

We conducted triaxial experiments on intact specimens of Westerly granite, a proxy for the continental crust. The experiments were performed at confining pressures ranging from 2 to 180 MPa to study the influence of crustal depth on the coalescence of microcracks up to macroscopic failure. Acoustic emissions and elastic wave velocities were monitored throughout the experiments, enabling a comprehensive description of the evolution in anisotropy and crack propagation. In a second step, we developed a micromechanical wing crack model coupled with the cracked solid theory to predict the evolution of elastic wave velocities towards the failure of brittle rocks. The predictions were compared to the experiments conducted at different confining pressures, and a strong correlation between modeled and measured velocities was observed. In addition, our estimates of the energy dissipated in inelastic processes through mechanical measurements is comparable with the energy dissipated in the creation of cracks explaining the measured variations in wave velocities. These results suggest that most of the energy dissipated toward the failure of specimens is related to crack propagation, and that our micromechanical model provides a good physical understanding of the failure of brittle rocks in terms of both damage and elastic wavespeed variations. Moreover, the significance of these inelastic energies indicate that precursory signs of failure might be observed. Therefore, we used our unified model to estimate the expected change in elastic velocities toward the failure of the brittle crust.

1 Introduction

The deformation of crystalline rocks is primarily accommodated by brittle mechanisms at shallow depths (up to 15-30 km depth [*Brace and Kohlstedt*, 1980]). In this regime, the nucleation, the development, and the coalescence of cracks can lead to the formation of faults, on which catastrophic failures can occur, such as devastating earthquakes. Therefore, understanding the development and the percolation of cracks in brittle materials is of major importance to assess seismic hazard. To this end, multiple theories and models have been proposed to better infer the deformation of the upper crust, as well as the development of damage in materials.

On the first hand, numerous experimental investigations have been conducted to explore the mechanical behavior of rocks leading up to macroscopic fault formation, with a particular focus on crystalline rocks [*Brace and Bombolakis*, 1963; *Lockner*, 1995]. Experiments showed that the brittle failure under compression is generally preceded by (figure 1a): i) first an initial closure of existing cracks as compression closes down existing defects, ii) an elastic regime where deformations are reversible, iii) the stable propagation of new cracks in the compression direction when stresses reach critical values on existing defects, iv) followed by their unstable development as their growth make it easier to propagate them further until they coalesce. The development of cracks causes non-linear behavior and create strong anisotropies [*Walsh*, 1965b,c,d]. v) Finally, localization takes place on a fault where frictional sliding occurs, during which is observed either a rapid release of strain energy, an earthquake in nature, or a slow continuous release of energy in aseismic slip.

On the second hand, these general mechanical observations have been performed through the observation of crack propagation in crystalline rocks. Crack propagation can be monitored through changes in various physical properties, including a change in elastic moduli, elastic wavespeed and rock attenuation, as well as by the onset of dilatancy and acoustic emissions. Specifically, an increase in crack damage has been observed to lead to a decrease in static moduli [*Brace and Bombolakis*, 1963; *Walsh*, 1965a]. In addition, seismic velocities are expected to decrease with increasing density of cracks in the material because cracks cause scattering and deflection of seismic waves, leading to longer travel times [*Nur and Simmons*, 1969; *Lockner et al.*, 1991, 1992; *Lockner*, 1993]. This scattering of seismic waves on defects generally lead to larger seismic attenuation as the absorption is increased by the number of cracks. Change in attenuation is also related to friction along cracks, which induces dissipation of the energy during the transmission of the elastic waves through inelastic processes activated during the elastic-wave induced strain perturbation [*Lockner et al.*, 1977].

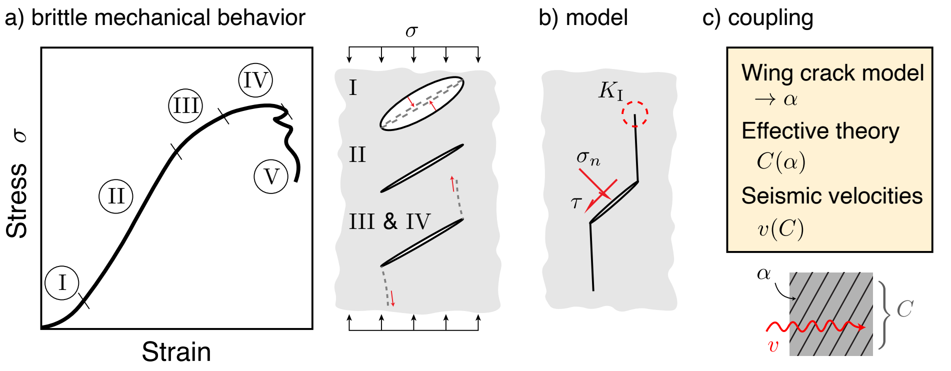

Figure 1. Framework of the article. a) Typical mechanical curve of a brittle solid exhibiting i) initial closure of cracks, ii) elastic phase, iii) stable and iv) unstable crack propagation, v) coalescence and frictional sliding. b) How the wing crack model boils down these mechanisms with linear elastic fracture mechanics for wings development, and friction on the crack surfaces. c) Proposed coupling of the article; as the model provides the crack geometry, crack densities α are linked and used to obtain the effective stiffness of the matrix C to estimate seismic velocities v. This coupling allows for continuous recording of brittle mechanisms toward failure thanks to velocity measurements.

To describe and quantify the mechanical behavior of brittle rocks, *Ashby and Sammis* [1990] developed a simple wing crack model. This micromechanical model considers homogeneously distributed penny-shaped cracks with friction on their surfaces and with wings that extend until their coalescence. This simplistic representation is particularly adapted to model brittle rocks because crystalline rocks exhibit these components toward failure at a microscopic level [*Tapponnier and Brace*, 1976]. To consider the three main components of matrix behavior, crack opening mechanisms and friction, this model combines different concepts such as (Figure 1b):

1. Elasticity theory for the matrix with its constants, the Young modulus E and the poisson ratio ν.
2. Mohr-Coulomb friction criterion on crack surfaces. The resistance to friction τ under a normal stress σ_n is:
$$\tau = \mu\sigma_n + c \tag{1}$$
where the two model parameters are μ the static friction coefficient, and c the cohesion.
3. Linear fracture mechanics to describe propagation of wings. Propagation occurs when the loading increases the stress concentration at the tip of a crack K_I and it reaches a material property, the fracture toughness K_Ic. So, we note:
$$K_\mathrm{I} = K_\mathrm{Ic} \tag{2}$$

These equations govern how the solid acts under any applied loading and how cracks will propagate. Failure of the rock is considered when the cracks grow enough to interact and finally coalesce. Due to its simplicity and adequacy, other authors have extended this model to consider different regimes of crack openings [*Deshpande and Evans*, 2008], the effect of loading rates [*Bhat et al.*, 2012], or subcritical crack growth [*Brantut et al.*, 2012]. Such micromechanical crack models have only been used for failure predictions. However, they also provide relevant information regarding the crack geometry and the evolution of damage during loading [*Basista and Gross*, 1998; *Bhat et al.*, 2011; *David et al.*, 2012, 2020a].

Importantly, it is also known that the development of damage under differential stress state induces anisotropy. Because of that, its theoretical effect on effective static and dynamic properties has been extensively studied [*Horii and Nemat-Nasser*, 1983; *Kachanov*, 1982a,b, 1992;

Sayers and Kachanov, 1995]. The effective theory of Sayers and Kachanov states that the anisotropy of rocks due to cracks can be expressed by crack density tensors. These tensors directly reduce the elastic properties as a function of crack growth and orientation. Therefore, if the cracks' geometry is known, the crack density tensors can be inverted, which allows evaluating directly the anisotropic moduli. In short, the effective theory provides a quantification of the anisotropic crack damage toward failure, plus it allows evaluating seismic velocities in any direction.

Despite these advances in both theories, there is currently no unified micromechanical model allowing for the prediction of the development of elastic anisotropy with wing-crack propagation in rocks. Indeed, the wing crack model could be linked with the effective theory to provide estimations of the evolution of elastic wave velocities toward the failure of brittle rocks. If this coupling is proven to be effective, the model could be used to estimate the evolution of in-situ stresses by monitoring the evolution of seismic velocities along the fault, excluding possible plastic or healing mechanisms (Figure 1c). Indeed, the analysis of seismic velocities variations has emerged as a promising tool to assess stress direction and evolution at depth in the crust [*Zoback and Zoback*, 1980; *Zoback et al.*, 1987; *Zoback and Zoback*, 1991; *Boness and Zoback*, 2006]. Since the evolution of stress in the Earth's crust is a key parameter controlling the occurrence of earthquakes, being able to monitor its evolution is of great importance to assess seismic hazard in a seismogenic area.

The goal of this work is to couple and test two of these theories, i.e., micromechanical model and effective medium theory, to evaluate how accurately they describe brittle mechanisms toward failure of brittle rocks. In particular, we will use a wing crack model to describe the evolution of seismic velocities for intact brittle rocks. To this end, laboratory triaxial experiments were conducted at different confining pressures on Westerly granite, a proxy of the continental crust behaving brittle. Elastic wave velocities were measured with various orientations, allowing to monitor the evolution of the elastic tensor toward the failure of the specimens using effective medium theory [*Sayers and Kachanov*, 1995]. In a second stage, these experimental results were compared to the predictions obtained using a unified micromechanical model, which allows for the estimation of the change in elastic properties toward the failure of brittle rocks. We demonstrate that both experimental and theoretical results are in good agreement, and that our micromechanical model can provide a good estimate of the elastic wave speed in brittle media. Furthermore, we show that in brittle rocks, most of the energy dissipated during crack propagation is related to dilatancy, as expected theoretically.

2 Methods

2.1 Sample and Apparatus

Cylinder samples of Westerly granite with a diameter of $d = 38$ [mm] and a height of $h = 81$ [mm] were loaded until failure in the triaxial apparatus called First, installed at the École Polytechnique Fédérale de Lausanne. An oil confining cell and a compensated axial piston applied the principal stresses $\sigma_1 > \sigma_2 = \sigma_3$. Five experiments were conducted at confining pressures of respectively 2, 12, 24, 72 and 180 [MPa]. The samples were protected from oil with a viton jacket and the pore pressure was null during the experiments. Experiments were conducted by imposing a constant injection rate of oil in the axial piston chamber, to guarantee a strain rate of about $\dot{\varepsilon} = 10^{-6}$ [s^{-1}]. Two axial LVDTs and up to eight strain gauges (four radial and four axial) were used to measure displacements and strains at an acquisition rate of 1 [Hz], respectively. From the LVDT and gauge measurements, axial and radial strains were averaged (ε_1 and ε_3).

2.2 Seismic Velocities

Fourteen piezoelectric transducers were placed around the rock sample, following the arrangement presented in Figure 2. Different piezoelectric transducers were used in this study to monitor both P- and S-wave velocities during experiments. This configuration maximized the variety of ray path angles. Regularly (around one hundred times per experiment), each transducer

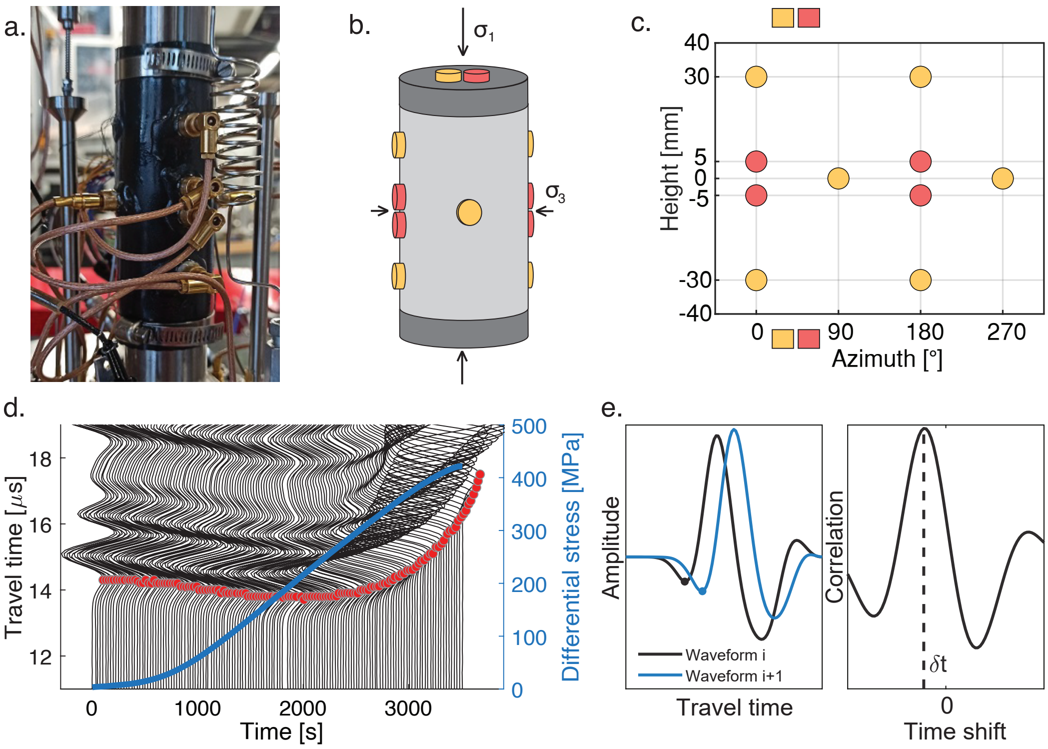

Figure 2. (a) Picture of the rock assemblage equipped with the sensors, (b) scheme of the sample assemblage and (c) sensor map in an azimuthal projection of the sample configuration and arrangement of piezoelectric sensors. P-waves and S-waves sensors are yellow and red, respectively. (d) Seismic waves evolution during loading (experiment WG5) derived from a pair of P-Waves sensors presenting a raypath angle of $35°$ angle). Red dots indicate the arrival time estimated automatically. (e) Cross-correlation method used to picked the first wave arrival. Waveforms number i and $i + 1$ are resampled for better accuracy, then passed through a Hann window to limit boundary effects. The similarity is computed, and the maximum correlation gives the time shift between the two waves.

emitted an electric signal while the others recorded reception at 10^7 [Hz]. We obtained ray paths with the following angles θ: P-waves: $0°$, $35°$, $52°$, $62°$, $90°$; S-waves: $90°$ horizontal and vertical.

Thanks to these seismic recordings, arrival times and propagation velocities were computed. The first arrival times of P and S-waves were initially hand-picked. The following ones were obtained with an iterative cross-correlation method [*Brantut et al.*, 2014] (see Figure 2e). If the correlation coefficient between two waveforms is below 0.9, the arrival time is hand-picked. For improved cross-correlation robustness, first wave peaks are picked. Then, the time interval between the wave arrival and the peak, which is approximately one-quarter of the wave period, is subtracted from the travel times. Note that the upper and lower sensors were placed inside the axial steel of the pistons to avoid stress localization. The travel time of elastic waves through the steel was subtracted as well. In seismic velocities computations, we assume that the velocities are transversely isotropic. This hypothesis supposedly remains valid until localization of cracks took place, which was only observed close to failure after peak stress is reached [*Lockner*, 1993]. Acoustic emissions (AE) caused by microseismicity were also complete recorded when five sensors reached an amplitude threshold. Then, the AE rate was computed with a moving average window of 120 seconds.

2.3 Seismic attenuation

Velocity surveys were also used to estimate the evolution of the seismic attenuation towards the failure of brittle rocks [*Lockner et al.*, 1977; *Paglialunga et al.*, 2021]. The attenuation was derived from the waveforms received on each pair of sensors corresponding to a given ray path angle θ. The amplitude reduction of the first wave arrival A is used as a proxy to study attenuation. Only P-wave attenuation is studied because S-wave first arrivals overlap with the P-wave seismic coda. To account for amplitude variations in each sensor, the measurements are normalized by their respective values under hydrostatic pressure as $A/A_h(\theta)$.

3 Experimental Results

3.1 Mechanical behavior

On the five experiments performed on Westerly granite, macroscopic failure is reached shortly after a peak in differential stress. After this peak, the deformations localize on a plane, i.e., fault formation, along which frictional sliding occurs until complete rupture of the sample and nearly total release of differential stress. Peak differential stress strongly increases with confining pressure, going from 199 MPa at 2 MPa confining pressure, to 1081 MPa at 180 MPa confining pressure (table 1). Moreover, the mechanical strain-stress curves document the processes towards failure of the samples. All mechanical curves on figure 3 exhibit similar features: first, they display an initially linear stage, where strains are reversible. On this so-called elastic region, the slope defines the elastic moduli of the material. The slope of $(\sigma_1 - \sigma_3) : \varepsilon_1$, the Young's modulus E_0, increases with confining pressure between 58 and 74 GPa. Meanwhile, the ratio of transverse and axial strains, the Poisson ratio ν_0, remains constant at an average of 0.30. These measurements are recapitulated in the table 1. Second, at approximately 70% of the peak differential stress, stress-strain curves deviate from linearity as more strains are accommodated. It coincides with the first acoustic emissions and the onset of dilatancy C'. This point C' is characterized by the maximum positive volumetric strain, and it also increases with increasing confining pressure. The reasons for this change to nonlinear mechanisms will be developed later, but crack propagation admittedly causes it. Initially a stable process, crack propagation becomes unstable as the spike in AE rate and the steep increase in strains both show, until failure. Finally, note that the axial strains towards failure are higher at high confining pressures, but the radial and volumetric strains do not show clear tendencies.

3.2 Evolution of the elastic wavespeed toward the brittle failure of specimens

The evolution of seismic velocities for all the different ray path angles is presented in Figure 4a. As seismic velocities are reduced by cracks intersecting the ray paths, their evolution is a proxy for crack propagation and orientation. We expect velocities perpendicular to the direction of crack growth to get reduced. Before applying differential stress, seismic velocities are nearly isotropic. The average initial v_p are ~ 4470, 4750, 4990, 5190, 5390 [m/s] and v_s are 2560, 2790, 2940, 2980, 3050 [m/s] at $\sigma_3 = 2$, 12, 24, 72 and 180 [MPa] respectively; it increases of up to 20% with confining pressure. Then, when differential stress is applied, velocities with ray path angles close to $0°$ with respect to σ_1 increase of up to 500 [m/s]. However, this effect is less noticeable with high confining pressure with changes of less than 200 [m/s], as observed for $\sigma_3 =$ 72 and 180 [MPa]. These increases of velocities are also gradual throughout the loading. Meanwhile, velocities with ray path angles close to $90°$ stay initially unchanged on all experiments. Upon reaching 50 to 70% of the peak differential stress, elastic wave speeds are reduced until rupture. Velocities are not reduced isotropically; with ray paths approaching a $90°$ angle, the velocity reductions are down to -25 to -35% depending on the experiment, while for $0°$ there is generally no reduction. This indicates that cracks mainly grow vertically in the direction of the principal stress. Variations to this rule are also discernible between tests. For instance, on $\sigma_3 =$ 12 and 24 [MPa], velocity variations are larger and reach -35%. In these tests, $v_{p,62^\circ}$ decreases more than $v_{p,90^\circ}$ close to failure, indicating possible diagonal coalescence of cracks. After fail-

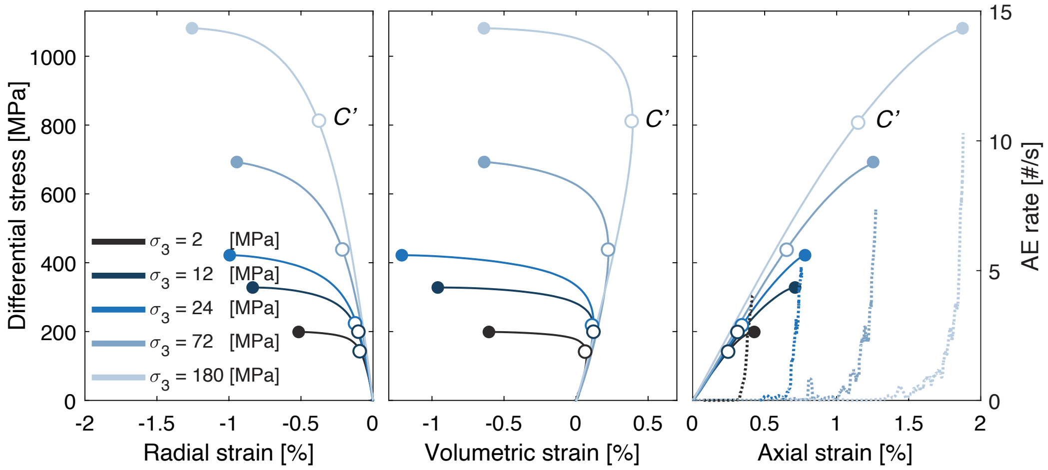

Figure 3. Evolution of (a) Radial, (b) volumetric and (c) axial strain with the differential stress for each experiment. The open symbol corresponds to the onset of dilation (C'). The full symbol; corresponds to the stress at which macroscopic failure occur. The evolution of acoustic emission rate is presented in panel c. The elastic phase (straight part of the curve) is followed by a stable crack propagation regime (first AE and softening of the curve) until unstable propagation happens (AE spike).

ure, most of the piezoelectric sensors detached, so velocity measurements are incomplete and not presented.

3.3 Estimate of the evolution of the crack densities

Crack densities are inverted from seismic velocities according to *Sayers and Kachanov* [1995]. Elastic wave velocities are directly correlated with elastic properties of rocks and their anisotropy. For a transversely isotropic medium, the P and S-wave velocities can be calculated in function of the ray path angle ϕ and the stiffness matrix C [*Brantut et al.*, 2011]:

$$\begin{aligned} v_p(\phi) &= [(C_{11}\sin^2\phi + C_{33}\cos^2\phi + C_{44} + \sqrt{M})/(2\rho)]^{1/2} \\ v_{s,v}(\phi) &= [(C_{11}\sin^2\phi + C_{33}\cos^2\phi + C_{44} - \sqrt{M})/(2\rho)]^{1/2} \\ v_{s,h}(\phi) &= [(C_{66}\sin^2\phi + C_{44}\cos^2\phi)/\rho]^{1/2} \end{aligned} \tag{3}$$

with the $\rho = 2650$ [kg/m^3] density of the medium and M defined as:

$$M = ((C_{11} - C_{44})\sin^2\phi - (C_{33} - C_{44})\cos^2\phi)^2 + ((C_{13} + C_{44})\sin 2\phi)^2 \tag{4}$$

The stiffness is a function of the elastic properties and the crack properties that *Sayers and Kachanov* [1995] describe with the second rank tensor of crack density α. For transversely isotropic cracks, they obtained:

$$\begin{aligned} C_{11} + C_{12} &= [(1/E_0) + \alpha_{33}]/D \\ C_{11} - C_{12} &= 1/[(1+\nu_0)/E_0 + \alpha_{11}] \\ C_{33} &= [(1-\nu_0)/E_0 + \alpha_{11}]/D \\ C_{44} &= 1/[2(1+\nu_0)/E_0 + \alpha_{11} + \alpha_{33}] \\ C_{13} &= -(\nu_0/E_0)/D \\ C_{66} &= 1/[(2(1+\nu_0)/E_0 + 2\alpha_{11}] \end{aligned} \tag{5}$$

with:

$$D = (1/E_0 + \alpha_{33})((1-\nu_0)/E_0 + \alpha_{11}) - 2(\nu_0/E_0)^2 \tag{6}$$

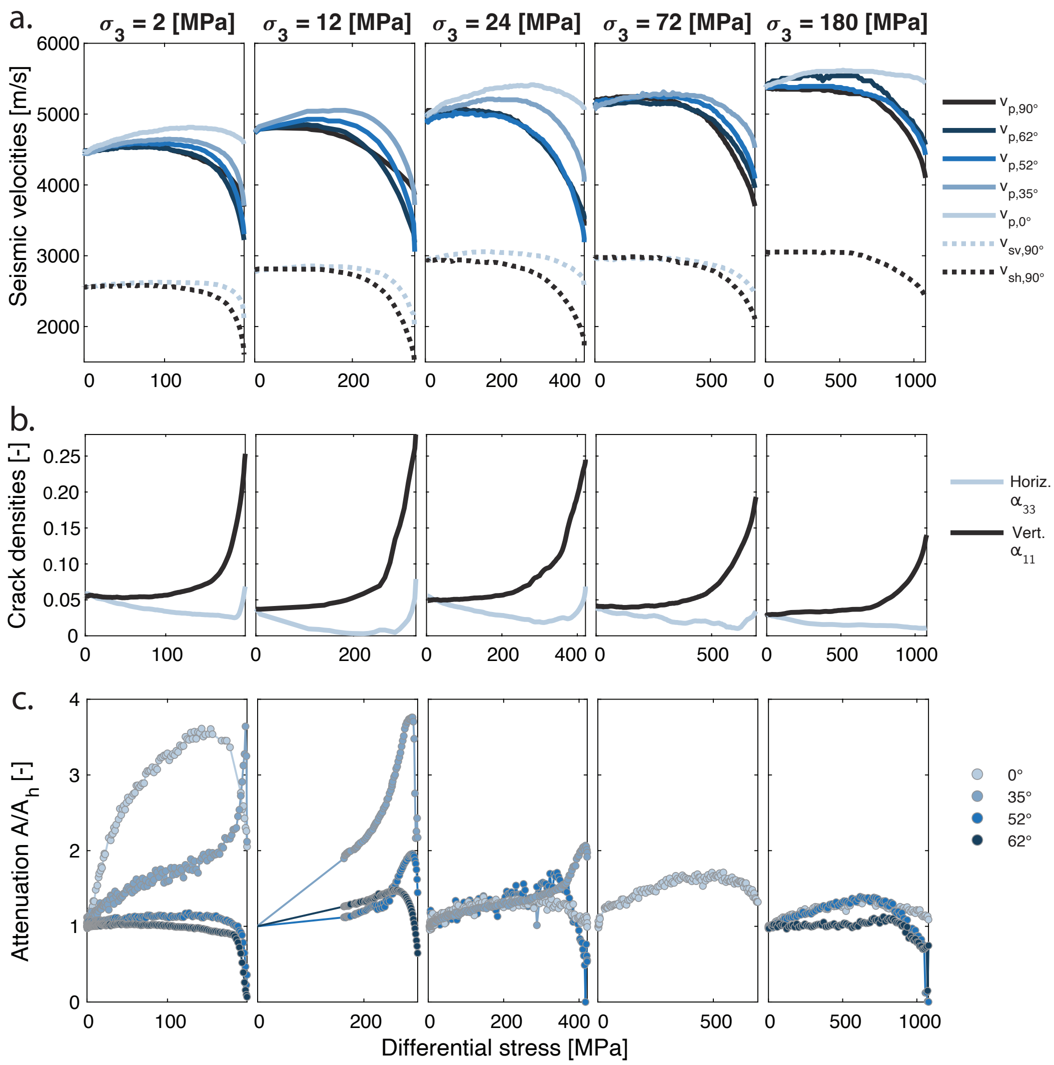

Figure 4. Evolution of a) seismic velocities, b) principal crack density components, and c) attenuation of the amplitude of the first seismic wave arrival. Confining pressure closes existing cracks, which increases hydrostatic velocities, decreases initial crack densities, and makes wave amplitude variations less sensitive. They all show that during each experiment, horizontal cracks (perpendicular to differential stress) get initially closed, then new cracks grow vertically (parallel to differential stress) exponentially until sample failure.

The second rank crack density tensor α is defined by:

$$\alpha = \frac{1}{V}\sum_{m=1}^{N}(a^3\mathbf{n}\times\mathbf{n})^{(m)} \tag{7}$$

For N circular cracks of respective radius $a^{(m)}$ in a volume V, where $\mathbf{n}^{(m)}$ is the unit normal to each crack. Assuming transversely isotropic damage, the principal values of this tensor are the vertical crack density α_{11} and the horizontal crack density α_{33}. The pair of values maximizing the likelihood between observed and theoretical speeds are kept as the components of the measured crack density.

The evolution of the principal components of crack densities are presented in Figure 4b. These curves allow for an easier and more detailed interpretation of crack propagation than seismic velocities. Initially, the crack distribution is nearly isotropic and the initial values of crack density decreases with increasing confining pressure, from 0.06 to 0.03 at $\sigma_3 = 2$ [MPa] and $\sigma_3 = 180$ [MPa], respectively. As the differential stress slowly increases, we observe an initial closure of horizontal cracks while the vertical crack densities remain unchanged. At high confining pressure, the horizontal crack density varies less, indicating that existing cracks are already closed. After a critical strength is reached during loading, crack nucleation begins and the vertical crack density grows exponentially until crack dilatancy leads to failure. This essentially proves that the cracks extend vertically in the direction of the principal stress σ_1. Although the number of experiments is limited, the peak crack densities seem to decrease with an increasing confining pressure, likely due to more localized damage at higher stresses. Finally, late horizontal crack opening is observed because of imminent failure.

Table 1. Table of the main results of the experiments

Test name	Confining pressure σ_3 [MPa]	Peak differential stress q_{peak} [MPa]	Young Modulus E_0 [GPa]	Poisson ratio ν_0 [-]
WG4	2	199	57.7	0.31
WG2	12	328	58.9	0.28
WG5	24	422	65.5	0.33
WG6	72	693	70.0	0.30
WG3	180	1081	73.7	0.28

3.4 Evolution of Attenuation During the Experiments

The evolution of attenuation throughout the experiments is analyzed for the different regimes identified before failure (i.e., initial closure of microcracks, elastic loading, and microfracturing).

The increase of differential loading (occurring in this configuration along the vertical direction) forces the closure of mainly horizontal cracks (Figure 4c, note that the experiment at $\sigma_3 = 12$ [MPa] has been replicated for improved attenuation data). Changes in horizontal crack density α_{33} are most likely to affect the direction parallel to the compression axis. This is confirmed by the seismic monitoring along the vertical direction; $A/A_h(0°)$ increases concurrently with a decrease of α_{33} in all the experiments. However, a clear dependence on the applied confining pressure σ_3 is observed, with peak values of $\sim$ 3.57, 1.34, 1.71, 1.31 for $\sigma_3 = 2$, 24, 72, 180 [MPa], respectively.

The other directions would also be affected by the closure of horizontal cracks, in proportion to their orientation. $A/A_h(35°)$ reveals itself to be highly affected by the decrease of α_{33}, notably increasing for small applied differential loads. As for the amplitude evolution in the vertical direction ($A/A_h(0°)$), $A/A_h(35°)$ increases during the closure of horizontal cracks and decreases with applied confining pressures. $A/A_h(52°)$ and $A/A_h(62°)$ show a slight increase during the closure of horizontal cracks. This behavior is similar for all the different applied σ_3. While for low σ_3 (in particular for $\sigma_3 = 2, 12$ [MPa]), a clear distinction between monitoring directions is observable, for higher σ_3 this distinction becomes less evident. For high σ_3, the increase in $A/A_h(\theta)$ is similar for all directions and reaches peak values of $\sim$ 1.3, 1.7, 1.3 for respectively $\sigma_3 =$ 24, 72, 180 [MPa], comparable to the values reached by $A/A_h(52°)$ and $A/A_h(62°)$ at low σ_3.

Then, in the purely elastic loading, attenuation remains essentially unchanged until crack nucleation occurs.

Once the critical strength of the sample is reached, crack nucleation begins and microcracks parallel to the compression axis start to grow (Figure 4c). The increase in the vertical crack density α_{11} is expected to mostly affect $A/A_h(\theta)$ in the directions perpendicular to the newly created cracks. This trend is confirmed for $A/A_h(52°)$ and $A/A_h(62°)$, which both decrease with increasing α_{11} for all the tested confining pressures. Unexpectedly, despite the increase of vertical cracks, $A/A_h(35°)$ keeps increasing up to the sample's proximity to failure (this behavior is, however, compatible with previous observations of compression tests [*Lockner et al.*, 1977]). Finally, the evolution of $A/A_h(0°)$ shows a decrease with increasing α_{11}, similar to the one observed for $A/A_h(52°)$ and $A/A_h(62°)$, but less pronounced in magnitude.

4 Modelling of the Experimental Results

4.1 Brittle Mechanisms

This experimental study provides a complete record of the influence of the confining pressure on the evolution of stresses, strains, and seismic velocities toward the failure of crystalline rocks. This data set is now used to calibrate a micromechanical model based on wing-crack theory from *Ashby and Sammis* [1990], coupled with effective medium theory, to attempt to predict both the brittle strain-stress behavior recorded during experiments and the evolution of seismic velocities during loading.

The rock sample is simplified to an elastic medium with homogeneously distributed cracks of identical geometry. The sample is submitted to a triaxial loading defined by the principal stresses σ_1 and $\sigma_2 = \sigma_3$, which impose a shear stress τ and normal stress σ_n on shear crack interfaces. Sliding along interfaces is assumed when the state of stress reaches a classical Mohr-Coulomb criterion, defined by a static friction coefficient μ and no cohesion. The geometry of cracks is simplified to N_V identical penny-shaped cracks of radius a, angle Ψ, and two wings of length ℓ as shown in Figure 5a, b. Since the granite is initially intact, the wings have no initial length ($\ell = 0$) and the number of cracks can be approximated to $N_V = \rho_c/a^3$, where ρ_c is the initial measured crack density.

Geometrically, the stresses acting on the cracks are:

$$\tau = \frac{\sigma_1 - \sigma_3}{2} \sin 2\Psi \tag{8}$$

$$\sigma_n = \frac{\sigma_1 + \sigma_3}{2} + \frac{\sigma_1 - \sigma_3}{2} \cos 2\Psi \tag{9}$$

The sum of the horizontal components of these stresses applied on a crack are defined as the wedging force:

$$F_w = (\tau + \mu\sigma_n)\pi a^2 \sin\Psi \tag{10}$$

For an implementation in a three-dimensional setting, Ashby and Sammis introduced this expression:

$$F_w = (A_1\sigma_1 - A_3\sigma_3)a^2 \tag{11}$$

Where A_1 and A_3 are:

$$A_1 = \pi\sqrt{\frac{\beta}{3}}(\sqrt{1-\mu^2} - \mu) \tag{12}$$

$$A_3 = A_1\frac{\sqrt{1+\mu^2}+\mu}{\sqrt{1+\mu^2}-\mu} \tag{13}$$

β is chosen to fit the beginning of crack propagation. This wedging force creates a mode I stress intensity factor, denoted K_{I}, at the tip of the crack, whose effective length is $\ell + \beta a$:

$$K_{\mathrm{I}} = \frac{F_w}{[\pi(\ell+\beta a)]^{3/2}} + \frac{2}{\pi}(\sigma_3 + \sigma_3^i)\sqrt{\pi\ell} \tag{14}$$

If $K_{\mathrm{I}} > K_{\mathrm{Ic}}$, the crack opens until $K_{\mathrm{I}} < K_{\mathrm{Ic}}$. To consider the effect of crack interaction, σ_3^i is an added internal stress that equilibrates the wedging force:

$$\sigma_3^i = \frac{F_w}{\Pi - \pi(\ell + a\cos\Psi)} \tag{15}$$

With the total crack area projected vertically $\pi(\ell + a\cos\Psi)$, and Π the area per crack:

$$\Pi = \pi^{1/3}\left(\frac{3}{4N_V}\right)^{2/3} \quad (16)$$

If $\Pi-\pi(\ell+a\cos\Psi)$ becomes negative, it means that the cracks coalesce and failure is reached.

The main parameters of this model are the initial crack density ρ_c, their radius a, the coefficient of friction μ, the fracture toughness K_{Ic} and β. We consider cracks with the orientation $\Psi = 45{+}1/2\arctan\mu$. In the literature, the fracture toughness of Westerly granite ranges from 1 to 2 [MPa m$^{1/2}$] [*Ashby and Sammis*, 1990; *Atkinson and Rawlings*, 1981; *Meredith and Atkinson*, 1985], so an average value of $K_{\mathrm{Ic}} = 1.5$ [MPa m$^{1/2}$] has been chosen. The size of initial cracks is estimated to be $a = 0.3$ [mm], which represents half of the average grain size of the granite. The initial crack densities were computed with seismic velocities recorded under hydrostatic stress conditions; a linear decrease in initial crack densities from 0.16 to 0.09 with increasing confining pressure was observed. The coefficient of friction $\mu = 0.65$ was chosen to fit the failure envelopes. Finally, β was defined using the onset of the crack opening process in the experiments at each confining pressure tested. We observed a general decrease in the crack opening process with increasing confining pressure, which justifies an increase in β with σ_3.

Table 2. Parameters of the wing crack model

Parameter	Value	Remark
K_{Ic}	1.5 [MPa m$^{1/2}$]	Average value in the literature
a	0.3 [mm]	Half of grain size
μ	0.65	Slope of the failure envelope
β	0.25 to 0.5	Increasing linearly with confining pressure
ρ_c	0.16 to 0.09	Decreasing linearly with confining pressure

The failure envelope estimated from these parameters (table 2) is presented in Figure 5c. Compared to the Hoek-Brown failure envelope, classically used in geotechnical engineering [*Cai*, 2010], the accuracy of the wing crack failure envelope is acceptable. The choice of parameters is critical for the wing crack model, yet each author evaluates them differently. For example, the size of the initial cracks is a sensitive parameter but hardly measurable; β has different definitions; and the fracture toughness of Westerly granite varies across studies.

Parameters of table 2 are now used in the micromechanical model to predict the evolution of strains measured experimentally. In elasticity, strains are linked to the strain energy density W:

$$\varepsilon_{ij} = \frac{\partial W}{\partial \sigma_{ij}} \quad (17)$$

W can be decomposed between the strain energy of the uncracked solid W_0, plus the strain energy of each crack ΔW:

$$W = W_0 + N_V \Delta W \quad (18)$$

Where:

$$W_0 = \frac{1}{2E_0}(\sigma_1^2 + 2\sigma_3^2(1-\nu_0)) \quad (19)$$

$$\Delta W = \frac{1}{E_0}\int_0^a K_{\mathrm{I}}^2 2\pi a da \quad (20)$$

K_{I} is substituted from Eq. 14, which allows evaluating ε_v. For ease of numerical implementation, the full development of *Deshpande and Evans* [2008]; *Nicolas et al.* [2017] is used to compute ΔW. Finally, as $\varepsilon_v = \varepsilon_1{+}2\varepsilon_3$, radial and axial strains are decomposed straightforwardly as the loading is imposed in axial displacement.

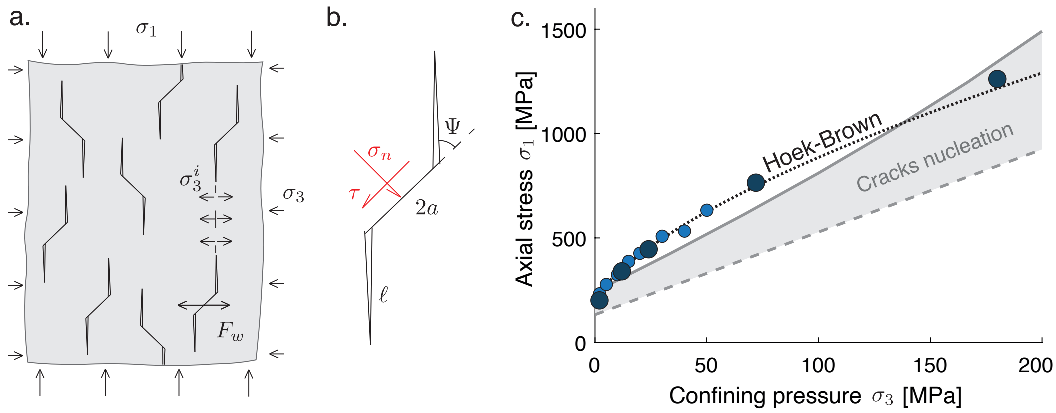

Figure 5. Geometry adopted for the wing crack model taken from [*Brantut et al.*, 2012; *Nicolas et al.*, 2017]. a. The rock is simplified to an elastic medium with homogeneously distributed cracks of identical geometry. b. Cracks are inclined penny shaped, slide on their face and extend vertically at its tips until they coalesce. The effect of cracks interaction is also considered with an internal stress σ_3^i that equilibrates the wedging force F_w. c. Experimental results (blue dots) used to fit the failure envelope of the wing crack model (in gray) and its crack nucleation process highlighted. Hoek and Brown failure envelope (dashed line) is also presented for comparison purposes.

Modelled radial, volumetric and axial strains are presented in figure 6 and compared to experimental results for each confining pressure tested. As shown, the model reasonably fits the mechanical behavior but does not capture accurately the softening of the axial strains as cracks only grow axially. In addition, experiments exhibited higher radial strains at lower confining pressures. These differences are probably related to our estimates of the parameters. For instance, different authors extended the wing crack model to include creep with subcritical crack growth [*Brantut et al.*, 2012] or different regimes of crack opening [*Deshpande and Evans*, 2008]. Integrating these extensions would bring supplementary parameter choices. However, we decided to keep the simplest form of the model in the following, since the prediction of the mechanical behavior remains close from our experimental observations.

4.2 Modelling of the Velocities From Brittle Mechanisms

To compute velocities from the wing crack model, Kachanov cracked solid theory was used. The crack density is obtained straightforwardly from its definition: $\rho_c = N_V a_{\text{eq}}^3$. As in section 3.3, we assume here a transversely isotropic cracks distribution, so that $\rho_c = 2\alpha_{11} + \alpha_{33}$. A simplification in the model compared to the experimental case is that the cracks only grow vertically in the wing crack model, while the horizontal crack density component stays unchanged. This simplification implies that only the vertical crack density increases with the propagation of wing cracks during the loading in axial stress, following:

$$\begin{aligned} \Delta\alpha_{11} &= \Delta\rho_c/2 = N_V(a_{\text{eq}}^3 - a^3)/2 \\ \Delta\alpha_{33} &= 0 \end{aligned} \tag{21}$$

where a_{eq} is the radius of an equivalent penny shaped crack composed by both the shear cracks and the associated wing cracks, defined geometrically by:

$$\begin{aligned} a_{\text{eq}} &= a\cos(\theta_{\text{eq}} - \Psi) + 2\ell\cos\theta_{\text{eq}} \\ \theta_{\text{eq}} &= \arctan\frac{\sin\Psi}{2\ell/a + \cos\Psi} \end{aligned} \tag{22}$$

In a second step, the theoretical estimates of $\Delta\alpha_{11}$ are used to estimate the evolution of the velocities with increasing differential stress, following the equations described in section 3.3.

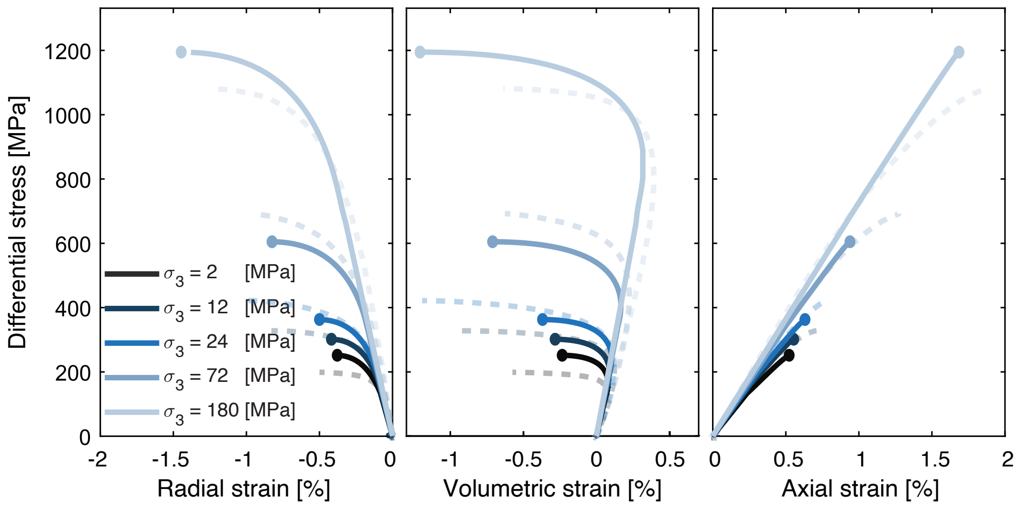

Figure 6. Radial, volumetric and axial strain stress plots of the model. Dashed lines are the experimental results and show where the model is inexact: radial strains are higher at low confining pressures and the model does not consider the propagation of horizontal cracks.

4.3 Accuracy of the micromechanical modelling

The modelled crack densities and velocities are directly compared with the experimental results. The figures 7a and b present our predictions of the evolution of $\Delta\alpha_{11}$ toward the failure of crystalline rocks for each confining pressure tested experimentally. A good correlation is globally observed between both experimental results and theoretical predictions. However, the theoretical estimate of the vertical crack densities are overestimated close to failure at the lower confining pressure tested, (at 2, 12 and 24 [MPa]).

Regarding seismic velocities, comparisons are presented in figures 7c and d. The figure 7c presents specifically the experiment conducted at $\sigma_3 = 72$ [MPa]. Here, $v_{p,35-90^\circ}$ are all modelled accurately with a sharp decrease of up to 30 %. However, a mismatch occurs for $v_{p,0^\circ}$ as the experimental velocities increase of 300 [m/s], while the modelled velocities remain nearly constant. The figure 7d allows making more general observations to understand these inconsistencies. Similarly to vertical crack densities, the elastic wave velocities generally diverge close to failure. At this stage, strain localization might occur, explaining the mismatch between experimental results and theoretical ones. In addition, significant deviations are observed when the ray paths are oriented close to 0° and before the crack nucleation, related to the fact that our model does not consider the closure and opening of horizontal cracks. Nevertheless, this simplification remains generally coherent, as the experimental horizontal crack density components have variations less than 0.05 (figure 4b).

The wing crack limitations addressed are: i) even though the wing crack model considers stress intensity factor at the defects, its failure envelope is similar in many aspects to a Mohr-Coulomb failure envelope in reason of shear on the crack surfaces. The envelope is close to a straight line, and most of the further limitations can be reduced to failure predictions uncertainties. ii) The wing crack model only considers vertical crack propagation, failing to take into account diagonal coalescence close to macroscopic failure and initial cracks closure. Seismic velocities can be predicted with the model, but with prudence when the cracks are not perpendicular to the ray path.

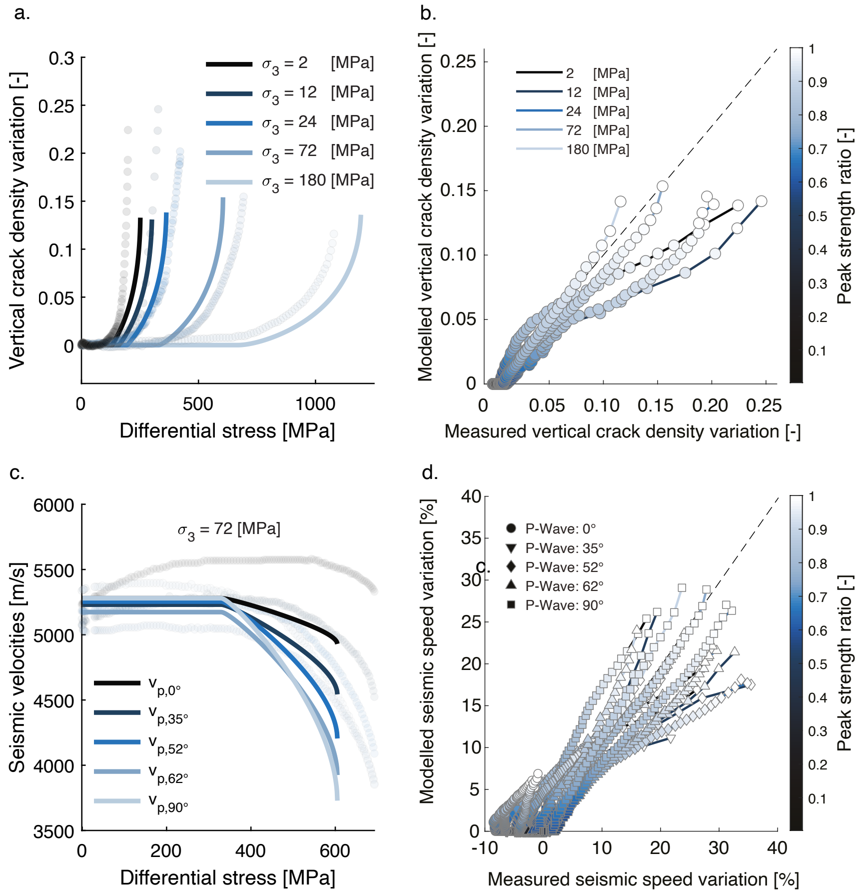

Figure 7. a. Evolution of the modelled vertical crack density during loading. Experimental results are in transparency. b. Direct comparison between the vertical crack density estimated for each velocity surveys and the one predicted using micromechanical model at the similar state of stress. The dashed line presents of slope of 1. The color bar corresponds to the stress state at which the surveys are performed. c. Modelled evolution of velocities during loading for the experiment conducted at 72 [MPa] confining pressure. Experimental results are presented in transparency to compare with the theoretical predictions. d. Direct comparison between experimental and modelled elastic wave speeds obtained at each velocity surveys. The color bar corresponds to the stress state at which the surveys are performed. The dashed line presents of slope of 1.

5 Discussion

This study provides experimental results and a model describing crack-induced anisotropy of brittle rocks toward their failure. Specifically, we studied the influence of confining pressure, which is a direct proxy of the depth in the crust. Therefore, the analysis of this full record can provide new insights of failure mechanisms potentially observable in crustal conditions.

We first discuss how confining pressure affects the crack development and induce anisotropic changes such as observed by seismic attenuation. Then, the validity of the wing crack model is analyzed through an energy budget that brings: i) a physical validation of the model, ii) details on which inelastic dissipative processes (i.e., dilatancy, new crack surfaces formation, shear sliding) are predominant in the brittle regime, and iii) comparison with energy dissipated during failure to discuss whether precursory elements of earthquakes can be observed with seismic velocity variations. Finally, we extrapolate the results of the model to estimate seismic velocities towards failure or brittle rocks in the crust.

5.1 Influence of confining pressure on crack induced-anisotropy and seismic attenuation toward the failure of crystalline rocks

The mechanical behavior of brittle solids is separated into the following regimes: i) initial closure of existing cracks, ii) purely elastic regime, iii) stable crack propagation, iv) unstable crack propagation, and v) failure. In our experiments (Figure 3), the initial closure due to deviatoric stress is barely detectable, as the confining pressure has already closed the majority of cracks. In the elastic stage, the increase of Young's modulus with confining pressure is explained by grains locking and by remaining crack closure, which both stiffen the rock matrix. Then, the non-linear strain hardening behavior is caused by the nucleation of new cracks and propagation of already existing cracks. Crystal plasticity can be excluded, as observed under these pressures on westerly granite [*Brace et al.*, 1966]. Crack opening is a dilatant process and requires a significant amount of energy and high stresses to open cracks at high confining pressure compared to low confining pressure. It explains why the onset of dilatancy, acoustic emissions, and crack nucleation occurs later at higher confining pressures [*Brace et al.*, 1966; *Lockner*, 1993; *Paterson and Wong*, 2005; *Browning et al.*, 2017]. Unstable crack propagation is highlighted by the change in sign of the volumetric strain evolution, which coincides with a peak of acoustic emissions. At this point, cracks get closer to each other, which makes their propagation unstable. Finally, macroscopic failure happens when cracks coalesce, forming a fault plane, with subsequent sliding along its plane. Until that fault slip, dilatancy is a key mechanism controlling the failure in intact brittle rocks.

While this analysis details the general mechanical behavior of a crystalline rock, it does not explain how cracks induce anisotropy, and affect seismic velocities and attenuation. Indeed, cracks can cause the seismic waves to scatter and change direction, plus they provide pathways for seismic energy to directly escape from the rock [*Lockner et al.*, 1977; *Paglialunga et al.*, 2021]. So, cracks oriented perpendicular to the direction of the wave will cause more attenuation and seismic reduction than those that are oriented parallel to the wave. These principles allow observing two conflicting mechanisms during the experiments: i) when a rock is under pressure, pressure causes the cracks to close or partially close, delaying the onset of nucleation of new cracks. This causes an increase of velocities, a reduction of attenuation, and a decrease in crack densities. Similarly, under the first stage of applied vertical loading, horizontal cracks close. Less crack development is also observed at higher confining pressures. ii) In opposition, new cracks will develop after a critical stress threshold. These new cracks will grow parallel to the main principal stress and consequently affect elastic properties. Perpendicularly to these new cracks, velocities are reduced, and attenuation is increased. However, close to complete failure of the samples, a late horizontal opening of cracks occurs. Wing cracks coalesce and interact with shear cracks, which induce an average orientation of the cracks at 30° with respect to the axial stress. The ratio v_p/v_s (90°) that is used to predict failure [*Gupta*, 1973] reach also its largest values at this stage of the experiments.

Seismic attenuation demonstrates a strong correlation with changes in the mechanical behavior leading to failure (Figure 4c). The energy impulse of a seismic wave passing through a slightly opened crack is expected to be sufficient for its closure, resulting in energy loss and increased attenuation [*Walsh*, 1966; *Lockner et al.*, 1977]. Conversely, when the crack is fully closed, no changes in attenuation are observed. In our study, we employed the monitoring of P-wave amplitude as a proxy for attenuation, where a decrease in P-wave amplitude corresponds to an increase in attenuation. At $\sigma_3 > 24$ MPa, a subtle increase in amplitude was observed, indicating the complete closure of the majority of cracks, thereby hindering the aforementioned dissipative mechanism. Of particular interest, an increase in amplitude was observed for cracks oriented at a 35° angle under lower confining pressures, coinciding with the sample's failure. This suggests that, at $\sigma_3 < 24$ MPa, diagonally-oriented cracks maintain a state between complete closure and full openness, allowing for frictional dissipation induced by seismic wave pulses. Similar observations have been reported in previous studies [*Lockner et al.*, 1977]. However, a detailed analysis of these variations is challenging, as they potentially overlap with the growth of new cracks, which produce the opposite effect. Nevertheless, these suggest that attenuation could be a tool to monitor the proximity to failure if recorded from different directions.

5.2 Dissipation of the energy during the failure of brittle rocks

Here, we examine the validity of the wing crack model by analyzing the energy budget associated with inelastic mechanisms leading to the failure of intact brittle rocks. By comparing the dissipated energies calculated using the experiments and the model, we assess its accuracy and identify the micromechanisms contributing to brittle failure.

During the experiments, the inelastic energy is directly obtained from strain and stress measurements, while the model also allows computing it from the variation of elastic wave speeds during the experiments.

From strain measurements, the energy dissipated inelastically per sample is simply: $w_d = w_{\mathrm{tot}} - w_e$, with w_{tot} the total strain energy and w_e the elastic strain energy; these energies can be directly computed from mechanical data as followed.

The total strain energy per sample is by definition:

$$w_{\mathrm{tot}} = \int \sigma_{ij} d\varepsilon_{ij} = \int \sigma_1 d\varepsilon_1 + 2 \int \sigma_3 d\varepsilon_3 \tag{23}$$

because $\sigma_{ij} = 0,\ \forall i \neq j$ in the eigenspace formed by the principal stresses σ_1, σ_2 and σ_3 (no shear stress is applied). The elastic strain energy is similarly obtained and as elastic strains are by definition linear, it simplifies to:

$$w_e = \frac{1}{2E_0}(\sigma_1^2 - \sigma_1\sigma_3 + 2\nu_0(\sigma_3^2 - \sigma_1\sigma_3)) \tag{24}$$

The inelastic strain energy of the sample w_d is scaled by the size of the initial sample to provide a comparable value: $W_d = hw_d$ [J/m^2]. The computation of W_d requires an array of strain measurements in reason of possible strain concentrations due to heterogeneous and non-linear rock behavior.

The loss of elastic wave speeds is linked to a loss of stiffness and the propagation of cracks, hence energy dissipated in crack propagation. Thus, the evolution of seismic velocities can be used to compute the stiffness loss and then, the crack strain energy. Let the crack strain be ε^c. The crack strain energy per sample is:

$$w_c = \int \sigma_{ij} d\varepsilon_{ij}^c \approx \frac{1}{2}\sigma_{ij}\varepsilon_{ij}^c \tag{25}$$

and $\varepsilon_{ij}^c = \Delta S_{ijkl}\sigma_{kl}$. This change of compliance is a function of the crack density tensor components [*Sayers and Kachanov*, 1995]. Accounting a damage zone $w = 20$ [mm] as observed by *Aben et al.* [2020] during failure thanks to localization of acoustic emissions and tomography imaging, the energy becomes $W_c \approx \frac{1}{2} w\sigma_{ij}\Delta S_{ijkl}\sigma_{kl}$ [J/m^2] [*Aben et al.*, 2019].

W_c and W_d exhibit similar trends and increase as the confining pressure rises (Figure 8a). These inelastic energies increase despite the creation of similar quantities of new crack surfaces (Figure 4b). Consequently, another pressure-sensitive process governs their behavior. Dilatancy, which is associated with crack opening and accurately captured by the model due to the similarity between W_c and W_d, emerges as the primary candidate. Consequently, in laboratory settings, variations in elastic wave speeds can be used to measure the dissipation of inelastic energies prior to failure.

Despite the general similarity, W_c is slightly lower than W_d. Indeed, other inelastic dissipation mechanisms that are not influencing velocity measurements or are not taken into account in the computation of W_c may take place. Intracrystalline plasticity and diffusive mass transfer are unlikely to occur under these conditions, but friction on crack surfaces may take place [*David et al.*, 2020b; *Brantut and Petit*, 2022], as suggested by the attenuation measurements. Clues of shearing can be seen when comparing in detail the energy dissipation in Figure 8b,c: with increasing confining pressure, W_d displays an initial plateau during loading, coming from shearing on cracks. Kachanov's theory does not consider inelastic shearing, so this plateau is absent for W_c. This results in shearing being observable in the larger mismatch between W_c and W_d at higher confining pressures. In short, the attenuation analysis and the energy budget both indicate there is negligible friction on crack faces below $\sigma_3 = 24$ [MPa].

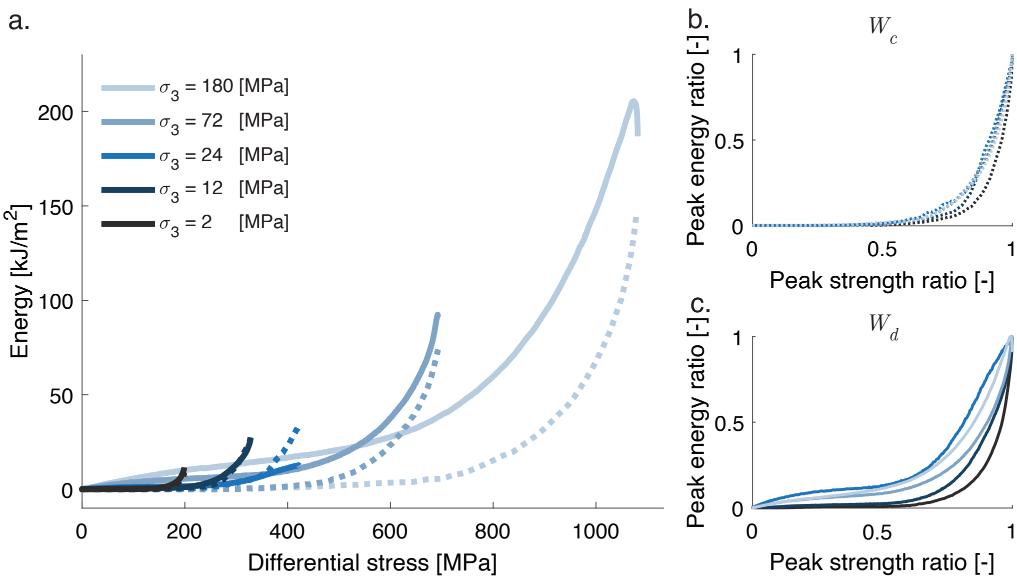

Figure 8. a. Evolution of crack opening energies in function of differential stress according to two methods. Dashed lines according to the stiffness loss associated with the evolution of seismic velocities (W_c), and full lines according to the strains and stress directly measured (W_d). b. and c. represent the same but normalized results for W_c and W_d respectively.

The energy dissipated into inelastic processes prior to the failure of intact rocks is significant in our experiments. Specifically, W_c and W_d increase from 20 to 200 kJ/m^2 with increasing confining pressure. Our theoretical estimates suggest that this energy could further increase at higher confining pressure, corresponding to greater depths. Remarkably, W_c and W_d are comparable to the values of breakdown work estimated during the failure of intact rocks, which refers to the energy dissipated during the weakening of faulting [*Wong*, 1982a; *Rummel et al.*, 1978]. These results show that almost the same amount of energy is lost during microcrack formation in the preliminary stage of fracture as during macroscopic failure of the specimen itself (Fig. 9). However, these comparisons hold only at the laboratory scale, where the damage zone prior to failure is roughly equivalent to the nucleation zone size. Scaling these findings to geological settings faces challenges due to the cyclic localization of the damage zone, leading to significant variations in its size [*Kato and Ben-Zion*, 2021]. Nevertheless, inelastic processes occurring during the nucleation of instability are expected to alter the nucleation processes and result in larger energetic ruptures [*Brantut and Viesca*, 2015]. Consequently, although the magnitude of these energies in real earthquakes remains unknown, the precursory inelastic energy, is expected to enhance the length scale of nucleation processes and improve our chances of detection. Therefore, we infer that precursory signs of failure may be observable through variations in elastic wave speeds, particularly at depth.

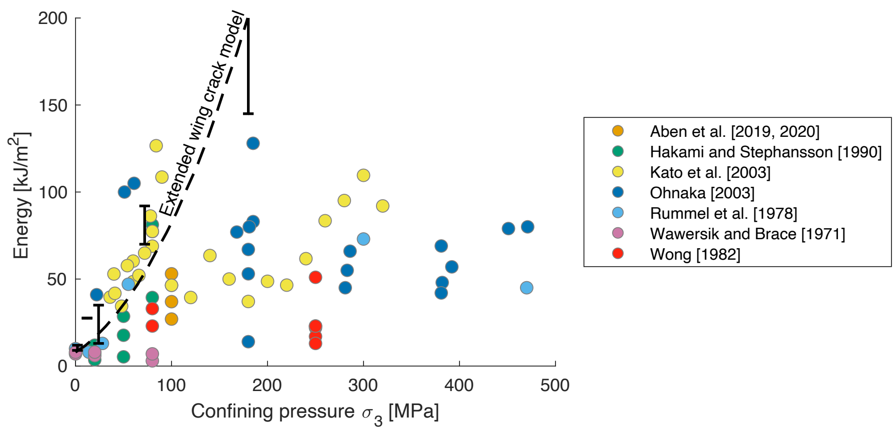

Figure 9. Comparisons between inelastic energy dissipated toward failure and during failure of granitoids in function of confining pressure. All circle points represent the breakdown work during macroscopic failure and slip on a main fault from *Wawersik and Brace* [1971]; *Rummel et al.* [1978]; *Wong* [1982b]; *Hakami and Stephansson* [1990]; *Ohnaka* [2003]; *Kato et al.* [2003]; *Aben et al.* [2019, 2020]. In black, our energy estimations before failure; the error bars show our measurements bounded by W_c and W_d. The dashed line represents modelled prediction according to the loss of seismic velocities.

5.3 Extrapolation to the Upper Crust

So, how are expected to evolve the elastic velocities in the earth crust prior to brutal failure? Indeed, the model and the experiments show a reduction of seismic velocities after a critical stress. As the model fits the velocity variations, it can be used to predict these losses for any given loading. The practicality of possible applications is demonstrated with a theoretical example where *in-situ* stresses are estimated based on elastic wave speed variations.

Let us consider an imaginary case with its principal effective stresses: $\sigma_3 = (\rho - \rho_w)gz$, with z the depth in the crust, ρ the rock density, ρ_w the water density, and g the gravitational force. σ_1 is the main stress acting horizontally (the differential stress is $q = \sigma_1 - \sigma_3$). For simplification purposes, let $\sigma_2 = \sigma_3$. As the model predicts the elastic wave speed variations for σ_1, Figure 10 is obtained. Elastic wave velocities are dependent on the Young modulus, and this parameter was estimated with the following empirical law (fitting our five Young Modulus measurements and velocity measurements of the initial pressure increase of WG3): $E_0(\sigma_3) = 3.75\log(\sigma_3 + 1) + 53.5$ [GPa]. The cracks open parallel to the principal stress, so the ray path angle is critical. With this graph, we can estimate the differential stress in relation to depth, ray path angle, and seismic speed reduction. Time-dependent effects such as subcritical crack growth or crack relaxation are not taken into account for this example.

This simple example shows that velocity reductions are principally perpendicularly to the main principal stress and at high differential stress. For instance, if we observe a 10% v_p reduction at a 5 [km] depth, it is associated with an applied 500 [MPa] differential stress. As crack induced anisotropy is a nearly reversible process, this differential stress inversion remains accurate despite the loading history for brittle rocks [*Bonnelye et al.*, 2017; *Passelègue et al.*, 2018]. Another factor to take into account in this interpretation is the size of the zone where new cracks are created. In geological settings, damage concentrates around faults in a so-called damage zone and its width varies with depth and tectonic settings. For instance, it can be kilometric at the surface on reverse faults, to decametric at depth [*Caine et al.*, 1996; *Mitchell and Faulkner*, 2009]. This width is crucial, as seismic variations will appear relatively smaller proportionally to the scale of observation. Therefore, variations at depth might get unnoticed despite important variations.

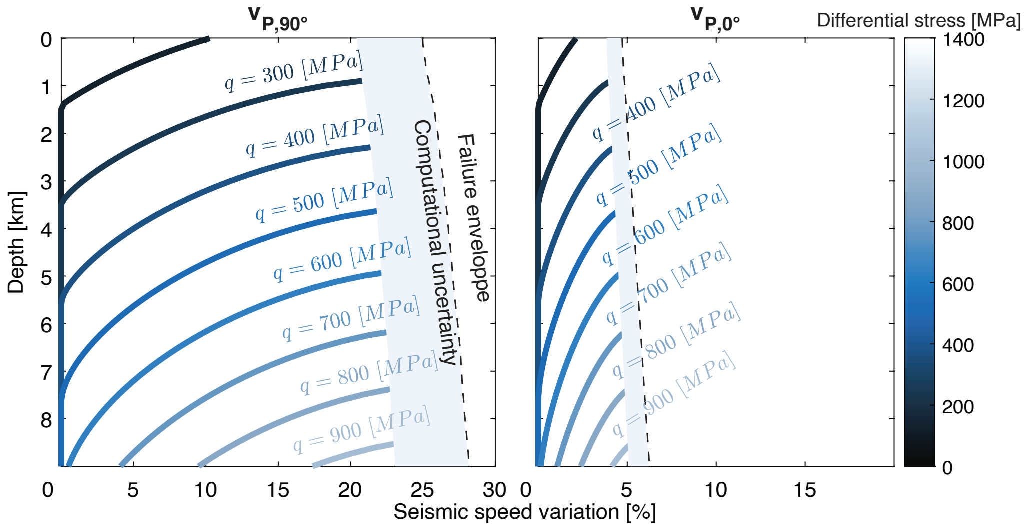

Figure 10. A wing crack model application to estimate elastic wave speed reductions in function of the principal stress σ_1, the angle between the ray path and σ_1, and the depth. For this example, σ_2 and σ_3 are computed in function of depth from a hydrostatic estimation of the stress.

In various studies monitoring the evolution of velocities in fault zones, velocity drops were observed after earthquakes followed by a post-seismic relaxation [*Brenguier et al.*, 2008]. The coseismic velocity reduction might be caused by coseismic damage and reopening of existing cracks. At first glance, these observations seem to contradict laboratory experiments and the model. However, by using the same method as Brenguier, it has also been observed that the earthquake velocity drop is reduced with depth [*Hobiger et al.*, 2012], which suggests that the drop is mainly caused by the reopening of existing cracks at low stresses [*Meyer et al.*, 2021; *Paglialunga et al.*, 2021]. As explained by fracture energy comparisons, our experiments are conducted on intact rocks, whose properties are different from fault zones or cracked solids. The strength of fault zones is generally low, so the crack nucleation process does not occur in stick-slip earthquakes at low depth [*Brace et al.*, 1966], meaning the wing crack model cannot be applied in these conditions. The model might still be applicable for intact rocks or at depth where cracks are healing.

6 Summary

1. Experiments on intact Westerly granite documented the evolution of crack nucleation with detailed elastic wave velocities and attenuation measurements. From damage inversion, we observed that cracks grow parallel to the principal stress, except close to failure at low confining pressures. Dilatancy is the main phenomenon controlling failure of intact brittle rocks. Shearing on cracks and defects only plays a critical role at high confining pressures (> 24 [MPa]).
2. The micromechanical wing crack model of *Ashby and Sammis* [1990], modified by *Deshpande and Evans* [2008], has been extended and linked to the cracked solid theory of *Sayers and Kachanov* [1995] with simple considerations on the cracks geometry. The model predicted the evolution of elastic wave velocities during loading of intact granite.
3. A budget of the energy dissipated to open cracks according to the mechanical results and the seismic velocities showed a compatibility with the use of the wing crack model with Kachanov's theory. Comparisons with literature estimates show that the inelastic energy dissipated prior to failure is of the same order as the breakdown work.

4. Therefore, the use of this model for geophysics applications is conceivable, but only at depth or for intact rocks. In-situ stresses and crack-induced anisotropy might be estimated with seismic velocities.

Acknowledgments

M.V. acknowledges support by the European Research Council Starting Grant project 757290-BEFINE.

References

Aben, F. M., N. Brantut, T. M. Mitchell, and E. C. David (2019), Rupture energetics in crustal rock from laboratory-scale seismic tomography, *Geophysical Research Letters*, *46*(13), 7337–7344, doi:https://doi.org/10.1029/2019GL083040.

Aben, F. M., N. Brantut, and T. M. Mitchell (2020), Off-fault damage characterization during and after experimental quasi-static and dynamic rupture in crustal rock from laboratory p wave tomography and microstructures, *Journal of Geophysical Research: Solid Earth*, *125*(8), e2020JB019,860, doi:https://doi.org/10.1029/2020JB019860.

Ashby, M., and C. Sammis (1990), The damage mechanics of brittle solids in compression, *Pure and Applied Geophysics*, *133*, 489–521, doi:10.1007/BF00878002.

Atkinson, B. K., and R. D. Rawlings (1981), *Acoustic Emission During Stress Corrosion Cracking in Rocks*, pp. 605–616, American Geophysical Union (AGU), doi: https://doi.org/10.1029/ME004p0605.

Basista, M., and D. Gross (1998), The sliding crack model of brittle deformation: an internal variable approach, *International Journal of Solids and Structures*, *35*(5-6), 487–509.

Bhat, H., C. Sammis, and A. Rosakis (2011), The micromechanics of westerley granite at large compressive loads, *Pure and Applied Geophysics*, *168*(12), 2181–2198.

Bhat, H. S., A. J. Rosakis, and C. G. Sammis (2012), A micromechanics based constitutive model for brittle failure at high strain rates, *Journal of Applied Mechanics*, *79*(3).

Boness, N. L., and M. D. Zoback (2006), Mapping stress and structurally controlled crustal shear velocity anisotropy in california, *Geology*, *34*(10), 825–828.

Bonnelye, A., A. Schubnel, C. David, P. Henry, Y. Guglielmi, C. Gout, A.-L. Fauchille, and P. Dick (2017), Strength anisotropy of shales deformed under uppermost crustal conditions, *Journal of Geophysical Research: Solid Earth*, *122*(1), 110–129, doi: 10.1002/2016jb013040.

Brace, W., and E. Bombolakis (1963), A note on brittle crack growth in compression, *Journal of Geophysical Research*, *68*(12), 3709–3713.

Brace, W., and D. Kohlstedt (1980), Limits on lithospheric stress imposed by laboratory experiments, *Journal of Geophysical Research: Solid Earth*, *85*(B11), 6248–6252.

Brace, W., B. Paulding Jr, and C. Scholz (1966), Dilatancy in the fracture of crystalline rocks, *Journal of Geophysical Research*, *71*(16), 3939–3953.

Brantut, N., and L. Petit (2022), Micromechanics of rock damage and its recovery in cyclic loading conditions, *Geophysical Journal International*, *233*(1), 145–161, doi: 10.1093/gji/ggac447.

Brantut, N., and R. C. Viesca (2015), Earthquake nucleation in intact or healed rocks, *Journal of Geophysical Research: Solid Earth*, *120*(1), 191–209, doi: https://doi.org/10.1002/2014JB011518.

Brantut, N., A. Schubnel, and Y. Guéguen (2011), Damage and rupture dynamics at the brittle-ductile transition: The case of gypsum, *Journal of Geophysical Research: Solid Earth*, *116*(B1).

Brantut, N., P. Baud, M. J. Heap, and P. G. Meredith (2012), Micromechanics of brittle creep in rocks, *Journal of Geophysical Research: Solid Earth*, *117*(B8), doi: https://doi.org/10.1029/2012JB009299.

Brantut, N., M. J. Heap, P. Baud, and P. G. Meredith (2014), Rate- and strain-dependent brittle deformation of rocks, *Journal of Geophysical Research: Solid Earth*, *119*(3), 1818–1836, doi:https://doi.org/10.1002/2013JB010448.

Brenguier, F., M. Campillo, C. Hadziioannou, N. M. Shapiro, R. M. Nadeau, and E. Larose (2008), Postseismic relaxation along the san andreas fault at parkfield from continuous seismological observations, *Science*, *321*(5895), 1478–1481, doi:10.1126/science.1160943.

Browning, J., P. G. Meredith, C. E. Stuart, D. Healy, S. Harland, and T. M. Mitchell (2017), Acoustic characterization of crack damage evolution in sandstone deformed under conventional and true triaxial loading, *Journal of Geophysical Research: Solid Earth*, *122*(6), 4395–4412, doi:10.1002/2016jb013646.

Cai, M. (2010), Practical estimates of tensile strength and hoek–brown strength parameter mi of brittle rocks, *Rock Mechanics and Rock Engineering*, *43*(2), 167–184, doi:10.1007/s00603-009-0053-1.

Caine, J. S., J. P. Evans, and C. B. Forster (1996), Fault zone architecture and permeability structure, *Geology*, *24*(11), 1025–1028, doi:10.1130/0091-7613(1996)024¡1025:FZAAPS¿2.3.CO;2.

David, E., N. Brantut, A. Schubnel, and R. W. Zimmerman (2012), Sliding crack model for nonlinearity and hysteresis in the uniaxial stress–strain curve of rock, *International Journal of Rock Mechanics and Mining Sciences*, *52*, 9–17.

David, E. C., N. Brantut, and G. Hirth (2020a), Sliding crack model for nonlinearity and hysteresis in the triaxial stress-strain curve of rock, and application to antigorite deformation, *Journal of Geophysical Research: Solid Earth*, *125*(10), e2019JB018,970.

David, E. C., N. Brantut, and G. Hirth (2020b), Sliding crack model for nonlinearity and hysteresis in the triaxial stress-strain curve of rock, and application to antigorite deformation, *Journal of Geophysical Research: Solid Earth*, *125*(10), e2019JB018,970, doi:https://doi.org/10.1029/2019JB018970.

Deshpande, V., and A. Evans (2008), Inelastic deformation and energy dissipation in ceramics: A mechanism-based constitutive model, *Journal of the Mechanics and Physics of Solids*, *56*(10), 3077 – 3100, doi:10.1016/j.jmps.2008.05.002.

Gupta, I. N. (1973), Premonitory variations in s-wave velocity anisotropy before earthquakes in nevada, *Science*, *182*(4117), 1129–1132, doi:10.1126/science.182.4117.1129.

Hakami, H., and O. Stephansson (1990), Shear fracture energy of stripa granite- results of controlled triaxial testing, *Engineering Fracture Mechanics*, *35*(4), 855–865, doi:https://doi.org/10.1016/0013-7944(90)90170-L.

Hobiger, M., U. Wegler, K. Shiomi, and H. Nakahara (2012), Coseismic and postseismic elastic wave velocity variations caused by the 2008 iwate-miyagi nairiku earthquake, japan, *Journal of Geophysical Research: Solid Earth*, *117*(B9), doi:https://doi.org/10.1029/2012JB009402.

Horii, H., and S. Nemat-Nasser (1983), Overall moduli of solids with microcracks: Load-induced anisotropy, *Journal of the Mechanics and Physics of Solids*, *31*(2), 155 – 171, doi:https://doi.org/10.1016/0022-5096(83)90048-0.

Kachanov, M. (1992), Effective Elastic Properties of Cracked Solids: Critical Review of Some Basic Concepts, *Applied Mechanics Reviews*, *45*(8), 304–335, doi:10.1115/1.3119761.

Kachanov, M. L. (1982a), A microcrack model of rock inelasticity part i: Frictional sliding on microcracks, *Mechanics of Materials*, *1*(1), 19 – 27, doi:https://doi.org/10.1016/0167-6636(82)90021-7.

Kachanov, M. L. (1982b), A microcrack model of rock inelasticity part ii: Propagation of microcracks, *Mechanics of Materials*, *1*(1), 29 – 41, doi:https://doi.org/10.1016/0167-6636(82)90022-9.

Kato, A., and Y. Ben-Zion (2021), The generation of large earthquakes, *Nature Reviews Earth & Environment*, *2*(1), 26–39, doi:10.1038/s43017-020-00108-w.

Kato, A., M. Ohnaka, and H. Mochizuki (2003), Constitutive properties for the shear failure of intact granite in seismogenic environments, *Journal of Geophysical Research: Solid Earth*, *108*(B1), doi:https://doi.org/10.1029/2001JB000791.

Lockner, D. (1993), The role of acoustic emission in the study of rock fracture, *International Journal of Rock Mechanics and Mining Sciences and Geomechanics Abstracts*, *30*(7), 883 – 899, doi:https://doi.org/10.1016/0148-9062(93)90041-B.

Lockner, D., J. Walsh, and J. Byerlee (1977), Changes in seismic velocity and attenuation during deformation of granite, *Journal of Geophysical Research*, *82*(33), 5374–5378.

Lockner, D., J. Byerlee, V. Kuksenko, A. Ponomarev, and A. Sidorin (1991), Quasi-static fault growth and shear fracture energy in granite, *Nature*, *350*(6313), 39–42.

Lockner, D., J. Byerlee, V. Kuksenko, A. Ponomarev, and A. Sidorin (1992), Observations of quasistatic fault growth from acoustic emissions, in *International geophysics*, vol. 51, pp. 3–31, Elsevier.

Lockner, D. A. (1995), Rock failure, *Rock physics and phase relations: A handbook of physical constants*, *3*, 127–147.

Meredith, P., and B. Atkinson (1985), Fracture toughness and subcritical crack growth during high-temperature tensile deformation of westerly granite and black gabbro, *Physics of the Earth and Planetary Interiors*, *39*(1), 33 – 51, doi:https://doi.org/10.1016/0031-9201(85)90113-X.

Meyer, G. G., N. Brantut, T. M. Mitchell, P. G. Meredith, and O. Plümper (2021), Time dependent mechanical crack closure as a potential rapid source of post-seismic wave speed recovery: Insights from experiments in carrara marble, *Journal of Geophysical Research: Solid Earth*, *126*(4), e2020JB021,301, doi:10.1029/2020JB021301, e2020JB021301 2020JB021301.

Mitchell, T., and D. Faulkner (2009), The nature and origin of off-fault damage surrounding strike-slip fault zones with a wide range of displacements: A field study from the atacama fault system, northern chile, *Journal of Structural Geology*, *31*(8), 802–816, doi:10.1016/j.jsg.2009.05.002.

Nicolas, A., J. Fortin, and Y. Guéguen (2017), Micromechanical constitutive model for low-temperature constant strain rate deformation of limestones in the brittle and semi-brittle regime, *Geophysical Journal International*, *211*(1), 300–321.

Nur, A., and G. Simmons (1969), Stress-induced velocity anisotropy in rock: An experimental study, *Journal of Geophysical Research*, *74*(27), 6667–6674.

Ohnaka, M. (2003), A constitutive scaling law and a unified comprehension for frictional slip failure, shear fracture of intact rock, and earthquake rupture, *Journal of Geophysical Research: Solid Earth*, *108*(B2), doi:https://doi.org/10.1029/2000JB000123.

Paglialunga, F., F. X. Passelègue, M. Acosta, and M. Violay (2021), Origin of the co-seismic variations of elastic properties in the crust: Insight from the laboratory, *Geophysical Research Letters*, *48*(12), e2021GL093,619, doi:10.1029/2021GL093619, e2021GL093619 2021GL093619.

Passelègue, F. X., L. Pimienta, D. Faulkner, A. Schubnel, J. Fortin, and Y. Guéguen (2018), Development and recovery of stress-induced elastic anisotropy during cyclic loading experiment on westerly granite, *Geophysical Research Letters*, *45*(16), 8156–8166.

Paterson, M. S., and T.-f. Wong (2005), *Experimental rock deformation: the brittle field*, vol. 348, Springer.

Rummel, F., H. J. Alheid, and C. Frohn (1978), Dilatancy and fracture induced velocity changes in rock and their relation to frictional sliding, *pure and applied geophysics*, *116*(4), 743–764, doi:10.1007/BF00876536.

Sayers, C. M., and M. Kachanov (1995), Microcrack-induced elastic wave anisotropy of brittle rocks, *Journal of Geophysical Research: Solid Earth*, *100*(B3), 4149–4156.

Tapponnier, P., and W. Brace (1976), Development of stress-induced microcracks in westerly granite, *International Journal of Rock Mechanics and Mining Sciences & Geomechanics Abstracts*, *13*(4), 103–112.

Walsh, J. (1965a), The effect of cracks on the uniaxial elastic compression of rocks, *Journal of Geophysical Research*, *70*(2), 399–411.

Walsh, J. B. (1965b), The effect of cracks on the uniaxial elastic compression of rocks, *Journal of Geophysical Research (1896-1977)*, *70*(2), 399–411, doi: https://doi.org/10.1029/JZ070i002p00399.

Walsh, J. B. (1965c), The effect of cracks in rocks on poisson's ratio, *Journal of Geophysical Research (1896-1977)*, *70*(20), 5249–5257, doi:https://doi.org/10.1029/JZ070i020p05249.

Walsh, J. B. (1965d), The effect of cracks on the compressibility of rock, *Journal of Geophysical Research (1896-1977)*, *70*(2), 381–389, doi: https://doi.org/10.1029/JZ070i002p00381.

Walsh, J. B. (1966), Seismic wave attenuation in rock due to friction, *Journal of Geophysical Research (1896-1977)*, *71*(10), 2591–2599, doi:10.1029/JZ071i010p02591.

Wawersik, W. R., and W. F. Brace (1971), Post-failure behavior of a granite and diabase, *Rock mechanics*, *3*(2), 61–85, doi:10.1007/BF01239627.

Wong, T.-f. (1982a), Shear fracture energy of westerly granite from post-failure behavior, *Journal of Geophysical Research: Solid Earth*, *87*(B2), 990–1000.

Wong, T.-F. (1982b), Effects of temperature and pressure on failure and post-failure behavior of westerly granite, *Mechanics of Materials*, *1*(1), 3–17, doi:https://doi.org/10.1016/0167-6636(82)90020-5.

Zoback, M. D., and M. L. Zoback (1991), Tectonic stress field of North America and relative plate motions, in *Neotectonics of North America*, vol. Decade Map 1, edited by D. B. Slemmons, E. R. Engdahl, M. D. Zoback, and D. D. Blackwell, p. 0, Geological Society of America, doi:10.1130/DNAG-CSMS-NEO.339.

Zoback, M. D., M. L. Zoback, V. S. Mount, J. Suppe, J. P. Eaton, J. H. Healy, D. Oppenheimer, P. Reasenberg, L. Jones, C. B. Raleigh, et al. (1987), New evidence on the state of stress of the san andreas fault system, *Science*, *238*(4830), 1105–1111.

Zoback, M. L., and M. D. Zoback (1980), Faulting patterns in north-central nevada and strength of the crust, *Journal of Geophysical Research: Solid Earth*, *85*(B1), 275–284.